

Opportunities and Challenges of Calendering Sulfide-Based Separators for Solid-State Batteries

Carina Amata Heck,^{*[a, c]} Timon Scharmann,^[b, c] Markus Osenberg,^[d] Alexander Diener,^[a, c] Ingo Manke,^[d] Peter Michalowski,^[a, c] and Arno Kwade^[a, c]

Continuous densification procedures such as calendering are crucial for sulfide-based solid-state batteries to realize industry-relevant processing. Therefore, in this study, the impact of line load, roller circumferential speed and roll temperature on slurry-based Li_3PS_4 and $\text{Li}_6\text{PS}_5\text{Cl}$ separators compacted by a lab-calender installed in an argon-gas-filled glovebox was investigated. While the Li_3PS_4 layers became fragile in calendered state, the tested $\text{Li}_6\text{PS}_5\text{Cl}$ separators were more suitable for calendering due to better mechanical stability. Besides basic analysis of, for example, density, length expansion, pore size distribution and specific ionic conductivity of the $\text{Li}_6\text{PS}_5\text{Cl}$ separators, 3D images of the structures were generated based on images obtained by synchrotron tomography. Here, all

calendered separators showed particle breakage of the $\text{Li}_6\text{PS}_5\text{Cl}$. A slight decrease of the specific ionic conductivity with increased applied line load or pressure was observed for calendering and uniaxial pressing, respectively. However, an increase in the conductivity was obtained for an increase in the stack pressure. In addition to poorer contact with the metal current collectors at low stack pressure, it is assumed that a spring back effect after densification could negatively affect the microstructure of the separator. These results highlight that a densification of binder-based $\text{Li}_6\text{PS}_5\text{Cl}$ separators does not necessarily result in improved ionic conductivity probably due to the individual deformation behavior of the materials used.

Introduction

Electrical energy storage devices such as lithium-ion batteries (LIBs) have become highly relevant these days to face the reduction of climatically critical CO_2 and NO_x emissions.^[1] Besides other approaches, alternative concepts like solid-state batteries (SSBs) are being considered to further extend the performance of LIBs.^[2–5] Here, the liquid electrolyte is replaced by a solid electrolyte potentially resulting in higher battery safety, as well as power and energy density due to the possibility of bipolar stacking and a potential application of lithium metal or silicon as anode.^[2,3,6] Because of their high ionic conductivity, sulfides are described as one of the most promising material classes for an application in SSBs.^[3,6] However, these materials are associated with a high sensitivity to moisture, which results in material degradation under the formation of toxic hydrogen sulfide (H_2S).^[6,7] Therefore, their

processing is commonly performed under an inert atmosphere, which makes it challenging to scale up.^[6,8] Only rare studies report its processing in a dry environment with dew points below $T_D = -50^\circ\text{C}$ for cell production yet.^[9,10] Moreover, continuous processes like extrusion for slurry preparation or calendering for densification must be evaluated and established to make production economically feasible.^[6,11–13] Regarding densification, current processing is mainly done by uniaxial pressing for pellet-type cells or slurry-based sheets.^[6,8,14,15] A study reports a densification by warm isostatic pressing of electrode and separator sealed in a laminate bag at 490 MPa.^[9] In the case of the separator, the reduction of porosity usually results in an improved particle contact and thus, an enhancement of the ionic conductivity due to the facilitation of lithium-ion flow via the solid structure.^[6,16] By hot-pressing Li_3PS_4 (LPS), for example, a relative density of 98% was achieved at 270 MPa and 200 °C near the glass transition temperature of the material.^[17] Moreover, a reduction of the separator thickness results in an increase of the specific energy density and a decrease of the internal resistance,^[18] as well as a reduction of the surface roughness is needed that modulates the contact between the electrode and separator.^[19] In the case of lithium metal as anode, high interfacial surface roughness facilitates short circuits due to a current focusing on sharper protrusions.^[19] Calendering itself (Figure 1) is used as continuous procedure for the preparation of sheets or films applied in various industries to achieve a uniform film with a target density. In recent decades, it has also been established as a compaction method for conventional LIB electrodes.^[1,20–24] In the case of sulfide-based SSBs, calendering is regarded as a promising way to uniformly reduce the porosity and surface roughness of electrodes and separators.^[6] One study reports a

[a] C. A. Heck, A. Diener, P. Michalowski, A. Kwade
Institute for Particle Technology, Technische Universität Braunschweig
E-mail: c.heck@tu-braunschweig.de

[b] T. Scharmann
Institute of Machine Tools and Production Technology, Technische Universität Braunschweig

[c] C. A. Heck, T. Scharmann, A. Diener, P. Michalowski, A. Kwade
Battery LabFactory Braunschweig, Technische Universität Braunschweig

[d] M. Osenberg, I. Manke
Helmholtz-Zentrum Berlin für Materialien und Energie

 Supporting information for this article is available on the WWW under
<https://doi.org/10.1002/batt.202300487>

 © 2024 The Authors. *Batteries & Supercaps* published by Wiley-VCH GmbH.
This is an open access article under the terms of the Creative Commons Attribution License, which permits use, distribution and reproduction in any medium, provided the original work is properly cited.

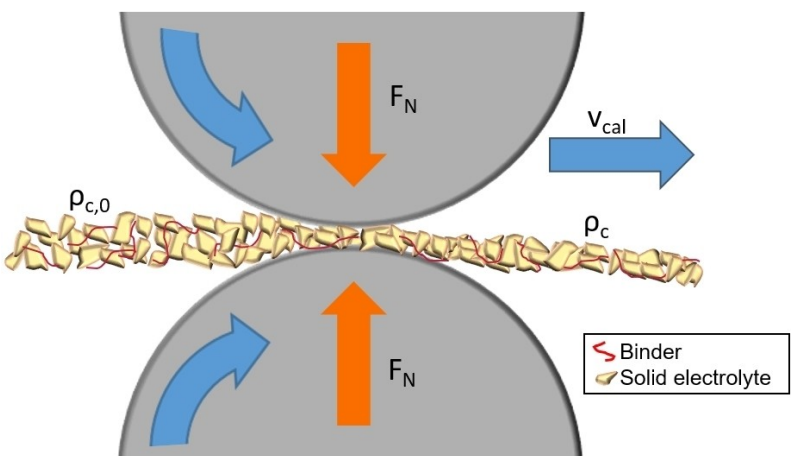


Figure 1. Schematic illustration of a two-roll calender adapted from Batzer and Heck et al., Ref. [6] under the terms of the CC-BY 4.0 license. Copyright: The Authors (2022), published by Wiley-VCH GmbH. $\rho_{c,0}$ describes the layer density before calendering and ρ_c afterwards. F_N is the rolling force and v_{cal} is the circumferential speed.

calendering of $\text{Li}_{10}\text{SnP}_2\text{S}_{12}$ -based sheets sealed in aluminum pouch bags outside a glovebox.^[25] Another study reports calendering of $\text{Li}_6\text{PS}_5\text{Cl}$ (LPSCI)-based separators to a thickness of less than 50 μm for an application in solid-state lithium-sulfur batteries, for example.^[26] Calendering is also reported for dry processing of sulfide-based SSBs.^[27,28] Separator layers can be coated directly onto one electrode^[8,13] or onto a release film to produce a free-standing sheet.^[25,29,30] In this case, the separator has to be laminated onto one electrode by calendering, for example.^[6] One benefit of this route over a direct coating onto one electrode is that a mutual dissolution of the binder by renewed contact with the solvent can be avoided.^[10,25] In addition, it should be mentioned that calendering has a direct influence on the mechanical properties of the separator. These resulting mechanical properties of the material are of great importance to ensure safety, reliability, performance and scalability in cell assembly. For example, if the electrolyte is brittle or extremely flexible, handling can be difficult or even lead to contamination during manufacturing. Robust mechanical properties, on the other hand, facilitate the processing, assembly and integration of sulfide separators in SSB cells. Apart from this, Meyer et al.^[21,31] found an exponential model equation (see Eq. 1) based on the equation of Heckel^[32] as a description of the compaction of conventional electrodes. The model was developed based on the determined coating density as a function of the applied line load.^[21]

$$\rho_c = \rho_{c,max} - (\rho_{c,max} - \rho_{c,0}) \exp(-\frac{q_L}{\gamma_c}) \quad (1)$$

Here, $\rho_{c,0}$ describes the coating density before calendering and ρ_c afterwards. $\rho_{c,max}$ is the maximum coating density, q_L describes the line load and γ_c the compaction resistance. The latter is highly dependent on the used materials, formulations, mass loading, as well as resulting pore structure within the coating.^[21,31] In the present study, the model was applied to the obtained coating density as a function of the line load for LPSCI

separator compaction (see Figure 4) for two different initial layer thicknesses.

Material and methods

Raw materials and general conditions

LPSCI (NEI Corporation) and β -LPS (NEI Corporation) were chosen as electrolyte materials, the particle size distributions and corresponding scanning electron microscopy (SEM) images of the powders are shown in Figure 2. LPS showed wide distribution with $d_{10} \approx 1 \mu\text{m}$, $d_{50} \approx 7 \mu\text{m}$ and $d_{90} \approx 40 \mu\text{m}$, while characteristic values for LPSCI are $d_{10} \approx 1 \mu\text{m}$, $d_{50} \approx 2 \mu\text{m}$ and $d_{90} \approx 7 \mu\text{m}$. For comparison of the two electrolyte materials, particle size distribution was measured by analytic centrifugation. Here, a slight underestimation of coarser particles should be considered due to premature sedimentation. The argyrodite LPSCI is associated with high ionic conductivity and lower costs compared to sulfide electrolytes with germanium such as $\text{Li}_{10}\text{GeP}_2\text{S}_{12}$.^[33,34] LPS provides the highest chemical stability among the $\text{Li}_2\text{S}-\text{P}_2\text{S}_5$ systems.^[35,36] However, it shows lower ionic conductivity compared to LPSCI amongst others because ion transport pathways are mainly two-dimensional, while lithium-ion mobility is facilitated in LPSCI because of three-dimensional cation pathways.^[37,38] As the binder, hydrogenated nitrile butadiene rubber (HNBR, Therban AT LT 2004, Arlanxeo Deutschland GmbH) and as solvent, p-xylene (Carl Roth GmbH & Co. KG) were used based on results of a former study.^[8]

Dispersing and coating of the separator slurry, calendering of the dried film, as well as measurements for density and porosity analysis were performed in an argon-filled glovebox (M. Braun Inertgas-Systeme GmbH). Moreover, sample preparation for particle size analysis, mercury intrusion measurements, SEM, nail penetration tests, tensile strength analysis, synchrotron tomography and electrochemical impedance spectroscopy (EIS) were carried out in an argon-filled glovebox.

Preparation of separators and calendering

The separator slurry was prepared by mixing the electrolyte powder in p-xylene for 30 min at a peripheral velocity of the disk equal to

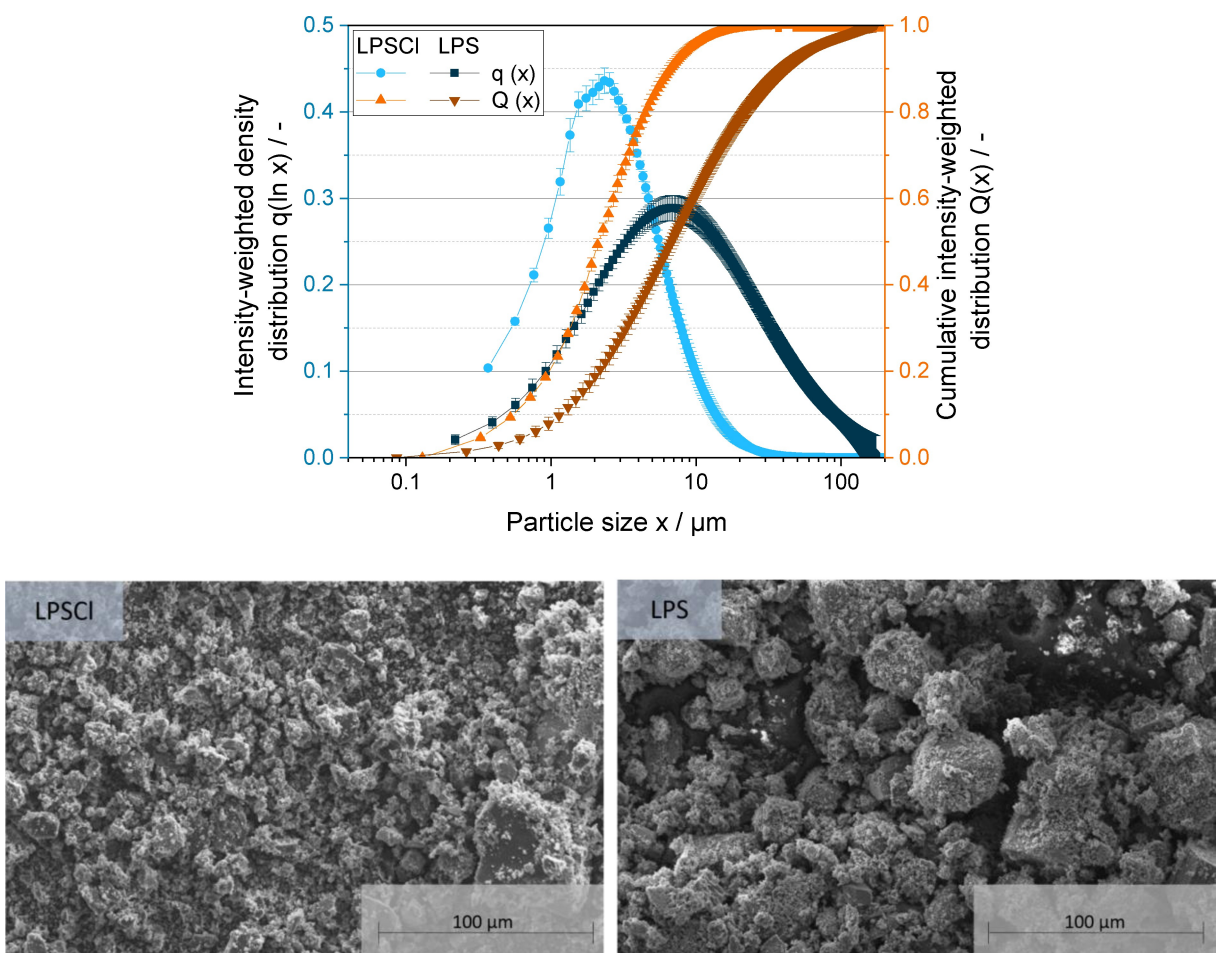


Figure 2. Particle size distribution of the LPSCI and LPS material and corresponding SEM images.

$v_p = 1 \text{ m s}^{-1}$ with a Dispermat CV3-PLUS dissolver (VMA-Getzmann GmbH) up to a solids content of 63.5 wt%, a binder content of 4.3 wt% and 95.7 wt% LPSCI. For LPS, working with a comparable solids content was not possible due to viscosity limitations, so a solids content of 30 wt%, but again a binder content of 4.3 wt% and LPS content of 95.7 wt% was chosen. Next, the slurry was dispersed at $v_p = 3 \text{ m s}^{-1}$ for 60 min. In the case of LPSCI, it was coated onto a siliconized polyester foil (PPI Adhesive Products GmbH) and in the case of LPS onto an aluminum foil (Speira GmbH), both by the doctor blade technique with a coating speed of $v_c = 10 \text{ mm s}^{-1}$ (Coatmaster 510, Erichsen GmbH & Co. KG) at room temperature. Finally, the layers were dried at room temperature overnight. Before calendering, the polyester foil of the LPSCI separators was removed.

Calendering was performed by a lab-scale two-roll calender (SUMET Technologies GmbH & Co. KG). The calendering rolls possess a diameter of 90 mm and a width of 150 mm. The electrolyte layers had a coating width of $w \approx 60 \text{ mm}$. Different line loads from 100 N mm^{-1} to 700 N mm^{-1} were applied. For each calendering, the minimum gap was set. Besides, different roll temperatures (40°C , 60°C , 80°C) and roller circumferential speeds (0.2 m min^{-1} , 1.0 m min^{-1} , 2.0 m min^{-1}) were investigated. To calculate the coating density, as well as the porosity three to six samples with a diameter of 16 mm were punched out and weighted by a fine balance (BCE224i-1S Entris II, Sartorius Lab Instruments GmbH & Co. KG). The thickness was measured by a tactile dial gauge (Mitutoyo). The coating density (ρ_c) and coating porosity (ε_c) were calculated

according to the equations described by Diener et al.^[24] The bulk density of the LPSCI electrolyte and HNBR binder were estimated to be 1.87 g cm^{-3} ^[39,40] and 0.96 g cm^{-3} , respectively. Hence, the density of the compound mixture in terms of binder and electrolyte was determined equal to 1.797 g cm^{-3} . The length of the LPSCI separators was measured manually before and after calendering and the resulting length expansion was calculated according to Equation (2) with L_i as the initial length of the separator in non-calendered state and L_a as the length after calendering:

$$\Delta \frac{L}{L} = \frac{L_a - L_i}{L_i} \quad (2)$$

The rate of compression Π was calculated according to Equation (3) with δ_a as layer thickness after calendering and δ_i as initial layer thickness in non-calendered state.^[23]

$$\Pi = 1 - \frac{\delta_a}{\delta_i} \quad (3)$$

The different analyses shown in this study are based on different slurry preparations probably with slight charge differences.

Additionally, LPSCI separators with a diameter of 16 mm coated onto an aluminum foil were compacted by a two-column lab press (PW 10, Paul-Otto Weber GmbH) within a press matrix. Applied pressure and temperature can be seen in Table 5. Samples were left

for 2 min within the press matrix for acclimatization and pressure was applied for 2 min afterwards.

Lab measurements

Particle size analysis: Intensity-weighted particle size distribution was determined by analytic centrifugation in a LUMiSizer measurement device (LUM GmbH). P-xylene with a HNBR-binder content of 4.5 wt% was prepared and 1 vol% of electrolyte powder was added. The sample was dispersed for 30 min in a dissolver to achieve a homogeneous mixture and filled into gas-tight cuvettes (LUM 2 mm, PA, Rect. Synthetic cell 110–134xx, LUM GmbH) after further dilution to achieve an initial transmission between 30% and 60%. A four-fold measurement was performed at ≈ 2300 g and 25 °C. Fitted and averaged distributions are shown.

Analysis of pore size distribution: The pore size distribution was analyzed by mercury intrusion (Quantachrome Instruments) according to Froboese et al.^[41]

Nail penetration test: Nail penetration tests were performed by a zwickiLine testing device (hereinafter referred to as Zwicki, ZwickRoell GmbH & Co. KG) under the usage of the testXpert III software. The Zwicki can apply a force up to 2.5 kN. A load cell with a maximum force of 500 N was used for carrying out the tests. The needle geometry used is in accordance with DIN 14477. This DIN deals with the determination of puncture resistance. The test speed was set at 1 mm min^{-1} to simulate a slow immersion of the needle tip, as well as possible and not to damage it permanently. A schematic illustration of the experimental setup is provided in the Supporting Information in Figure S.1. The tests were conducted in a dry room at 20 °C and a dew point of the supply air of $T_D = -60^\circ\text{C}$.

Tensile strength measurement: In analogy to the nail penetration tests, tensile tests were performed by Zwicki and the testXpert III software. The same load cell was used as for the nail penetration tests. An example of a sample used for this measurement is shown in the Supporting Information in Figure S.2. The travel speed was set to 1 mm min^{-1} to prevent tearing of the film. The tests were performed in a dry room at 20 °C and a dew point of the supply air of $T_D = -60^\circ\text{C}$.

Scanning electron microscopy (SEM): For SEM analysis, an SEM Phenom XL (Thermo Fisher Scientific Inc.) was used. For imaging a primary beam voltage of 10 kV (LPSCI) or 15 kV (LPS) was used and a vacuum pressure of 0.1 Pa in the SEM sample chamber was applied. The device is placed in a dry room with supply air's dew point of $T_D = -27^\circ\text{C}$. Exposition to the dry room atmosphere was kept to a minimum.

Electrochemical impedance spectroscopy (EIS): For EIS measurement, the separator sample was placed between two sealed stainless steel plungers in a PTFE tubing with a diameter of 16 mm.^[8,13] For measurement series 1, 2 and 5 a cell press device was used for an application of 25 MPa stack pressure. For series 3, 4 and 6 stack pressure was applied by a manual hydraulic press (MP250D, MAASEN GmbH). EIS measurement was performed in a climate chamber (SU-242, ESPEC) at 25 °C. Before measurement, the prepared samples were taken out of the glovebox and left in the climate chamber for 20 min for acclimatization. Applied stack pressure is shown in Table 5 for different measurement series. For the analysis, a potentiostat (Zennium, ZAHNER-Elektrik GmbH & Co. KG) was used. A frequency range from 4 MHz to 10 Hz in potentiostatic mode was applied. For the determination of the ionic resistance, the analysis software RelaxIS 3 (rhd instruments GmbH & Co. KG) was used evaluating a frequency range of 4 kHz to 4 MHz.

Synchrotron tomography: Synchrotron tomography was performed at the BAMline,^[42] a beamline at the BESSY II facility. The same set of parameters have been used for each tomography. The samples have been fixated on top of aluminum rods to allow for stable mounting on the rotation stage at the BAMline end station. The X-ray spectra for transmission-based measurements have been conditioned using a W/Si-based double multilayer monochromator. This resulted in an incident beam with an energy of 25 keV. The spectral peak width was approximately 200 eV. The beam transmitted through the sample containing the absorption information was then converted to visible light using a CdWO₄ scintillator. The light signal was then magnified with 20x microscope optics and detected with a pco.edge 5.5. The whole setup resulted in a field of view of $0.92 \times 0.78 \text{ mm}^2$ with a pixel size of 0.36 μm . During the measurements, the samples were continuously rotated through 180 degrees while 2500 radiographic projections were taken. Before and after the measurements, 40 flat fields have been acquired. The exposure time was 0.3 s, and a complete measurement took 13 minutes.

For data post-processing, Python was used for calculations and ImageJ/Fiji^[43,44] for data inspection. The flat field normalized radiograms were first denoised using a total variation filter. For reconstruction, the filtered back projection implemented in the astra toolbox^[45,46] was applied to the normalized and denoised image stack. During this processing step, the ring filter was applied. The final 3D reconstruction was then denoised again using total variation. The 3D structures shown in Figure 11 were generated using GeoDict (Math2Market GmbH) and the threshold for binarization was calibrated according to the geometrically determined porosity. Color-based segmentation of selected cross-sections was performed by Matlab (TheMathWorks, Inc.) based on manually set thresholds.

Results and discussion

Comparison of LPS and LPSCI calendering behavior

Slurry-based LPSCI and LPS layers were produced for calendering. A solids content of 63.5 wt% could be realized for LPSCI slurries, while for LPS only 30 wt% due to viscosity limitations. For LPSCI, free-standing layers could be produced with sufficiently high mechanical stability for subsequent analysis. However, for LPS, free-standing layers could not be achieved due to high brittleness. Therefore, to investigate the impact of calendering on LPS, it was coated onto aluminum foil. After calendering, it became fragile and detached from the aluminum foil independently of the roller circumferential speed. Strong damage to the layer was found for a roll temperature of 80 °C. Obtained layers and corresponding SEM images are shown in Figure 3. The achieved layer thicknesses before and after calendering, as well as the rate of compression for both LPS and LPSCI are shown in Table 1.

While for LPS higher initial layer thicknesses were observed, lower thicknesses result after densification compared to LPSCI. This is mainly due to the lower solids content used for LPS slurry in comparison to LPSCI slurry.^[8] Because of the higher amount of solvent used for LPS separators, more evaporation paths within the fresh-coated slurry are built up during slurry drying. Thus, a higher amount of voids resulted in a higher initial thickness compared to LPSCI separators. This is confirmed

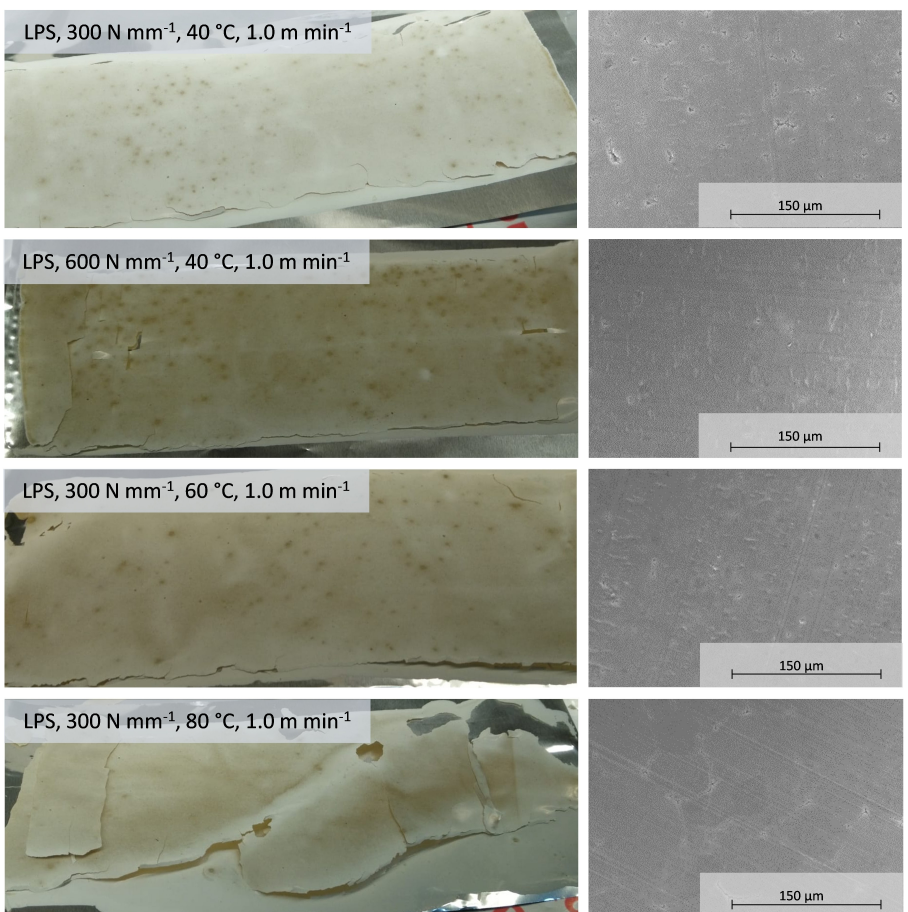


Figure 3. Examples of LPS layers in calendered state and corresponding SEM images.

Table 1. Layer thicknesses before and after calendering and rate of compression for LPS (30 wt % solids content, 4.3 wt % binder and 95.7 wt % LPS) and LPSCI (63.5 wt % solids content, 4.3 wt % binder and 95.7 wt % LPSCI) based separators. Thickness calendered at 80 °C was partly not determinable (n. d.) due to high fragility or strong layer defects. For the determination of the layer thickness, ten measurements were taken distributed over the entire separator layer except for the peripheral zones directly before and after calendering.

| Line load/ N mm ⁻¹ | Roll temp./°C | Roller circumferential speed/m min ⁻¹ | Thickness before calendering/μm | | Thickness after calendering/μm | | Rate of compression/- | |
|----------------------------------|------------------|--|------------------------------------|-------|-----------------------------------|-------|-----------------------|-------|
| | | | LPS | LPSCI | LPS | LPSCI | LPS | LPSCI |
| 200 | 40 | 1.0 | – | 219±4 | – | 164±3 | – | 0.25 |
| 300 | 40 | 1.0 | 279±16 | 221±4 | 99±6 | 160±3 | 0.64 | 0.28 |
| 400 | 40 | 1.0 | – | 219±3 | – | 156±1 | – | 0.29 |
| 500 | 40 | 1.0 | – | 218±3 | – | 151±2 | – | 0.31 |
| 600 | 40 | 1.0 | 279±26 | 219±4 | 88±6 | 151±2 | 0.68 | 0.31 |
| 700 | 40 | 1.0 | – | 217±2 | – | 151±2 | – | 0.30 |
| 300 | 60 | 0.2 | – | 216±4 | – | 144±3 | – | 0.34 |
| 300 | 60 | 1.0 | 281±24 | 214±5 | 89±3 | 155±2 | 0.68 | 0.28 |
| 300 | 60 | 2.0 | – | 221±3 | – | 161±6 | – | 0.27 |
| 300 | 80 | 0.2 | – | 217±3 | – | n. d. | – | n. d. |
| 300 | 80 | 1.0 | 281±25 | 215±3 | n. d. | 137±5 | n. d. | 0.36 |
| 300 | 80 | 2.0 | – | 209±3 | – | 136±3 | – | 0.35 |

by porosity measurement. For LPS in non-calendered state a porosity of 76±4% was obtained, while for LPSCI a porosity of only 37±2% was achieved. Consequently, due to the lower

amount of solid material per volume in non-calendered state a lower thickness and higher rate of compression is achieved for LPS after calendering compared to LPSCI. Further analysis of

LPS separators in calendered state such as determination of porosity was prevented due to the high fragility of the samples. Low fracture toughness despite low stiffness has already been reported for electrolytes of the Li₂S-P₂S₅ type.^[47]

Also, within the LPS layers dark spots can be seen presenting large particles (probably ~100 µm and greater) exposed to stronger stress compared to small particles during calendering to achieve homogeneous layer thickness. The strong deformation of these particles could additionally result in strong local interlocking and tension within the layer. To obtain a deeper understanding of the different mechanical behavior of LPS and LPSCI, further analysis in terms of plastic and elastic deformation or X-ray diffraction analysis should be performed for different densification states. For further investigations within this study, LPSCI was found more suitable for calendering compared to LPS, among others because of the mechanically more stable separators.

Further investigations on calendering LPSCI separators

Coating density and pore size distribution were analyzed for different line loads, roller circumferential speeds and roll temperatures of the free-standing LPSCI separators. In Figure 4 a), the coating density as a function of the line load is shown for a basis weight of $b_L = 14 \text{ mg cm}^{-2}$ and $b_L = 24 \text{ mg cm}^{-2}$. Roll temperature and speed were set to 40 °C and 1.0 m min⁻¹. As expected, increasing line load resulted in an increase of the coating density with an approximation to a maximum value determined by load and weight limits.^[48] For the highest applied line load of 700 N mm⁻¹ for $b_L = 24 \text{ mg cm}^{-2}$ a coating density of 1.60 g cm⁻³ and porosity of 11% was determined. In comparison, the coating density in non-calendered state is ≈1.15 g cm⁻³ and the porosity is ≈37%.

The theoretical density of the compound mixture in terms of binder and electrolyte is 1.797 g cm⁻³. For $b_L = 14 \text{ mg cm}^{-2}$, a

coating density equal to 1.54 g cm⁻³ and a porosity of 14% was achieved for 600 N mm⁻¹. Thus, increasing the initial coating height results in a slightly higher coating density and lower porosity, respectively.^[24,31] Obtained porosities are shown in Table 2.

An increase in coating height results in an increase of voids between the individual particles and thus, more space is available for particles to escape in during densification, as well as low marginal effects occur.^[24] Moreover, particle breakage and plastic deformation of the individual components affect the achievable maximum coating density.^[24] In general, lower porosity of the separator results in improved particle contact and thus, an improved ionic conductivity.^[16] Contrariwise, a reduction of the initial separator thickness is aimed to minimize the battery cell's internal resistance, weight and costs, as well as to maximize the energy density.^[18,49,50] To describe the experimental results, the model according to Meyer et al.^[21] was applied. Approximation parameters are shown in Table 3. A compaction resistance of 91 N mm⁻¹ was determined for layers with a basis weight of 14 mg cm⁻² and of 128 N mm⁻¹ for a basis weight of 24 mg cm⁻². Increased compaction resistance for increasing the basis weight is in line with the results of Meyer et al.^[31] Because of the higher amount of particles within the layer, more friction between the particles must be overcome during densification leading to higher compaction resistance.^[31] Due to the higher mechanical stability of the separators, all subsequent tests were carried out with separators with a basis weight of $b_L \approx 24 \text{ mg cm}^{-2}$.

Moreover, the impact of roll temperature for 40 °C, 60 °C and 80 °C and roller circumferential speeds of 0.2 m min⁻¹, 1.0 m min⁻¹ and 2.0 m min⁻¹ were investigated, while the line load was kept constant at 300 N mm⁻¹. For samples calendered at 80 °C and 0.2 m min⁻¹, reliable measurements could not be performed due to strong mechanical damages of the layer. The resulting coating densities are presented in Figure 4b). In the case of 40 °C and 60 °C, no significant difference was obtained

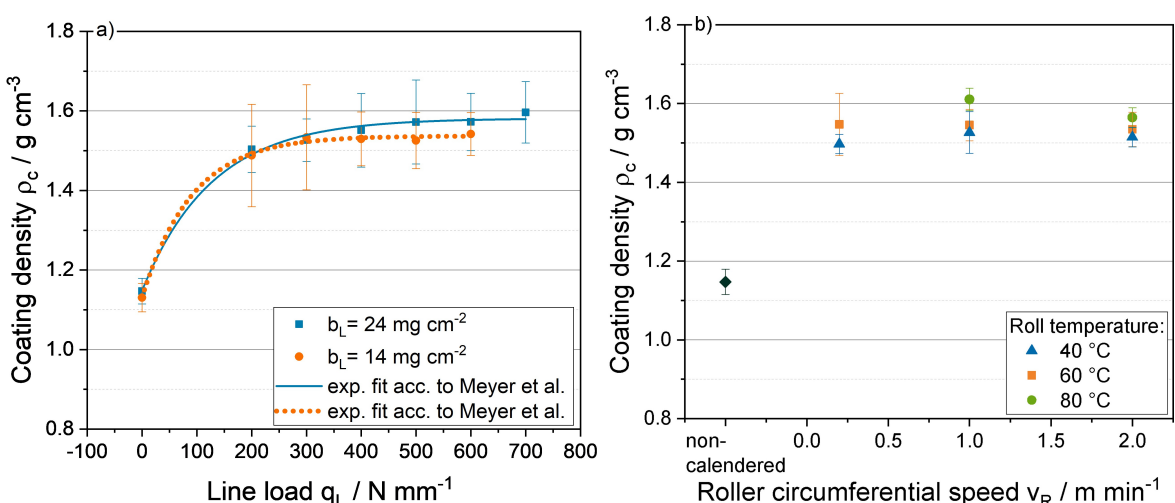


Figure 4. a) Coating density as a function of the line load for LPSCI separators. Calendering was performed at a roll temperature of 40 °C and a roller circumferential speed of 1.0 m min⁻¹. b) Coating density as a function of the roller circumferential speed for LPSCI separators calendered at different roll temperatures. Calendering was performed at 300 N mm⁻¹. Error bars represent the standard deviation based on the mass and thickness variation on at least three samples.

Table 2. Porosity of LPSCI separators calendered at different line loads, roll temperatures and roller circumferential speeds for different basis weights. Standard deviation on at least three samples is presented based on the variation of mass and layer thickness.

| Line load/ N mm ⁻¹ | Roller circumferential speed/m min ⁻¹ | Roll temp./°C | Porosity/% $b_L = 14 \text{ mg cm}^{-2}$ | Porosity/% $b_L = 24 \text{ mg cm}^{-2}$ |
|----------------------------------|---|---------------|---|---|
| 200 | 1.0 | 40 | 17±7 | 16±3 |
| 300 | 1.0 | 40 | 15±7 | 15±3 |
| 400 | 1.0 | 40 | 15±4 | 14±5 |
| 500 | 1.0 | 40 | 15±4 | 13±6 |
| 600 | 1.0 | 40 | 14±3 | 12±4 |
| 700 | 1.0 | 40 | — | 11±4 |
| 300 | 0.2 | 40 | — | 17±2 |
| 300 | 2.0 | 40 | — | 16±2 |
| 300 | 0.2 | 60 | — | 14±4 |
| 300 | 1.0 | 60 | — | 14±3 |
| 300 | 2.0 | 60 | — | 15±3 |
| 300 | 1.0 | 80 | — | 10±3 |
| 300 | 2.0 | 80 | — | 13±3 |

Table 3. Approximation parameters according to the model of Meyer et al.^[21] for different basis weights of the LPSCI separator.

| Basis weight $b_L / \text{mg cm}^{-2}$ | 14±2 | 24±2 |
|---|-----------|-----------|
| Initial coating density $\rho_{c,0} / \text{g cm}^{-3}$ | 1.13±0.01 | 1.15±0.01 |
| Maximal coating density $\rho_{c,max} / \text{g cm}^{-3}$ | 1.54±0.01 | 1.58±0.01 |
| Compaction resistance $\gamma_c / \text{N mm}^{-1}$ | 91±11 | 128±15 |

upon changing the roller circumferential speed. For 80 °C, a slight increase in the coating density with a decrease in the roller circumferential speed can be assumed. Here, the highest density was achieved for 80 °C and 1.0 m min⁻¹ with 1.61 g cm⁻³. For the elastomeric HNBR binder used in this study a low Mooney viscosity as a characteristic quantity of rubbers^[51] of 39 MU at 100 °C is described, indicating that a softening of the binder may have caused a denser structure at 80 °C. In addition, a softening of the sulfide particles is assumed especially at the separator surface (see SEM images).

In general, increased fragmentation of the separators was observed with increasing roll temperature and decreasing roller circumferential speed (see Figure 5). This is probably also reinforced by an increase in the line load. Accordingly, the length expansion of the separators rises for an increase in roll temperature and a decrease in roller circumferential speed (see Figure 6a)). The increase in temperature probably decreases the stiffness of the binder and/or electrolyte particles. On the other side, a decrease in speed increases the time at which tension acts on the separator between the rolls and, because of the viscoelastic binder behavior, enlarges the strain. Also, an increase in line load has a slight impact on length expansion. Strong deformation of the separator in the calender gap in combination with length expansion probably results in tension fragmentation of the layer. To minimize such strong fragmentation, also gap size variations and multiple calendering should

be investigated in the future. Also, the elastic spring back of the separators after leaving the roll gap for different line loads, roll temperatures and speeds via, for example, direct roll-gap detection should be examined.^[24] In conclusion, achieving high density at 80 °C and 1.0 m min⁻¹ comes with the trade-off of severe destruction of the electrolyte layer, as it has already been observed for a calendering of LPS (see Figure 3). For comparison, separators calendered at 40 °C are shown in the Supporting Information in Figure S.3.

The pore size distribution determined by mercury intrusion is shown as a function of the line load in Figure 6b). It should be considered that the diameter within the pore throat is determined and only accessible pores can be measured by mercury intrusion.^[41]

As expected, increasing the line load results in a reduction of pore size, confirming a defined densification of the separators. For non-calendered samples and samples calendered at 100 N mm⁻¹ the pore size distribution is bimodal, while in the case of 400 N mm⁻¹ and 600 N mm⁻¹ unimodal distributions were obtained. Here, small pores in the range of 0.01 µm to 0.03 µm present in the non-calendered state and separator calendered at 100 N mm⁻¹ probably representing the inner porosity of the LPSCI material appear to be closed for 400 N mm⁻¹ and 600 N mm⁻¹.

Tensile strength and nail penetration analysis

For the nail penetration test, samples calendered at different line loads and a roller circumferential speed of 1.0 m min⁻¹ and roll temperature of 40 °C were investigated. The results are shown in Figure 7a). By increasing the line load, the absorbed nail force is enhanced, while the deformation is reduced. For example, the non-calendered separator allows deformation of

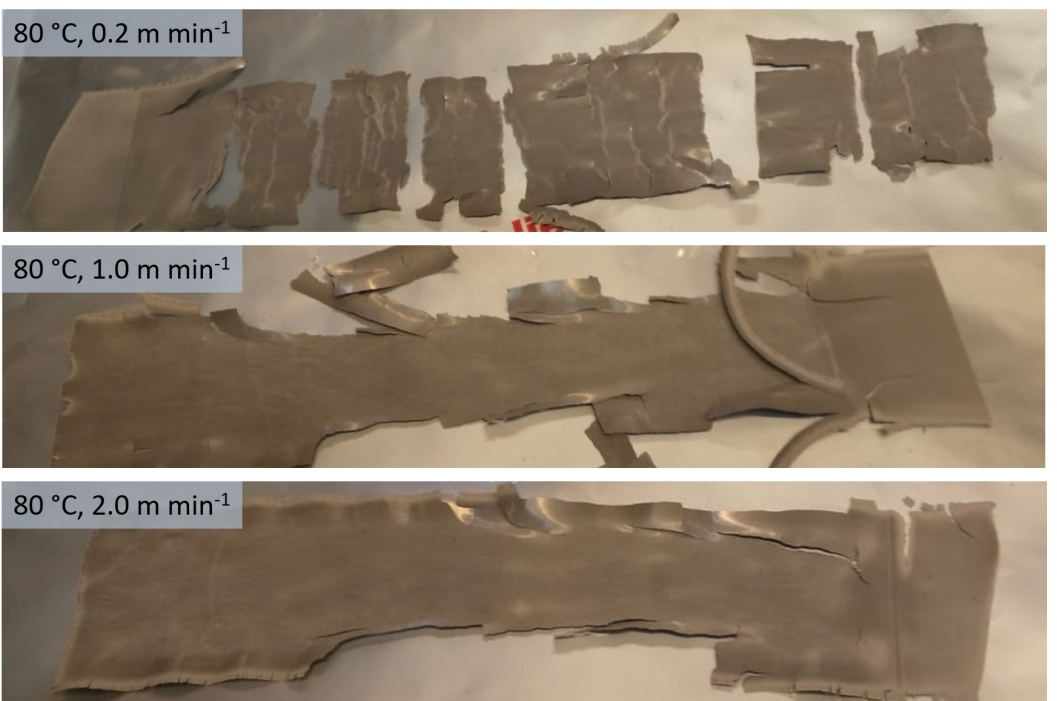


Figure 5. Examples of separators calendered at 80 °C and different roller circumferential speeds.

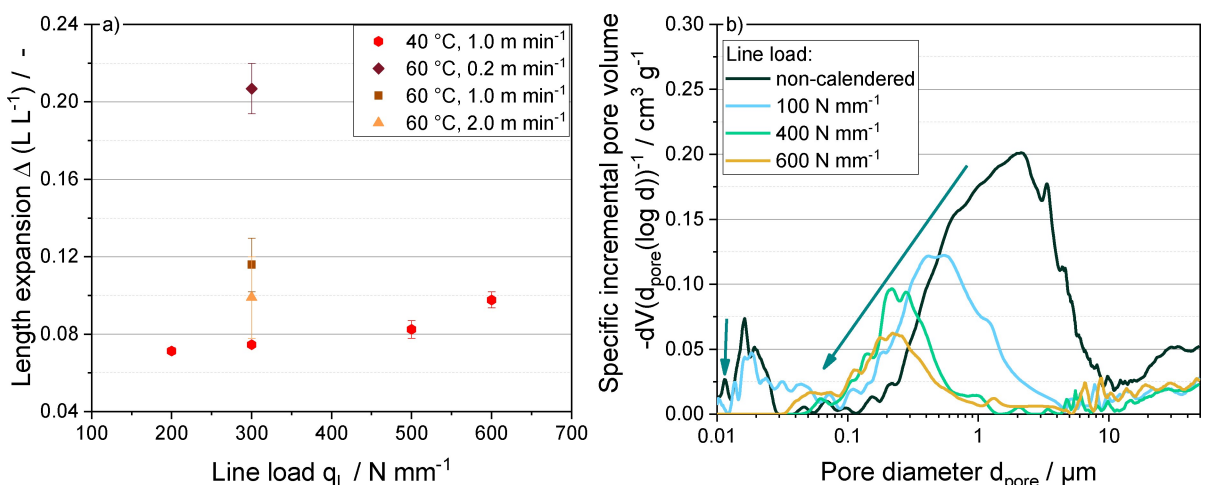


Figure 6. a) Length expansion of LPSCl separators as a function of the applied line load. Error bars represent the standard deviation on three samples. b) Pore size distribution for different line loads. Calendering was performed at a roll temperature of 40 °C and a roller circumferential speed of 1.0 m min⁻¹.

about 1.15 mm during nail penetration until it is penetrated at an applied force of about 0.14 N. The maximum force was absorbed at a line load of 600 $N \text{ mm}^{-1}$ with an applied force of 0.255 N and a resulting deformation of 0.68 mm. These results indicate a plastic deformation of separators during calendering at line loads of 300 $N \text{ mm}^{-1}$ or higher. This plastic deformation is the reason for the subsequent lower deformation and higher load during the nail penetration tests. Thus, the application of a high line load such as 600 $N \text{ mm}^{-1}$ is beneficial as it leads to a denser structure that is more resistant to mechanical stress.

Additionally, tensile tests were performed for both non-calendered and calendered samples at different line loads, as

shown in Figure 7b). In analogy to the nail penetration test, the layers exhibit the characteristic of an increase in applied stress with an increase in line load value, while the resulting elongation decreases. For the non-calendered material, the elastic limit is about 20 $N \text{ cm}^{-2}$. The maximum tension was reached at a line load of 500 $N \text{ mm}^{-1}$ with above 120 $N \text{ cm}^{-2}$. In addition, no initial plastic deformation was detected at a line load of 100 $N \text{ mm}^{-1}$. As the line load increased, the elongation of the material during the tensile test only slightly decreased, while its mechanical strength increased significantly. In the future, one challenge will be to achieve high tensile strength

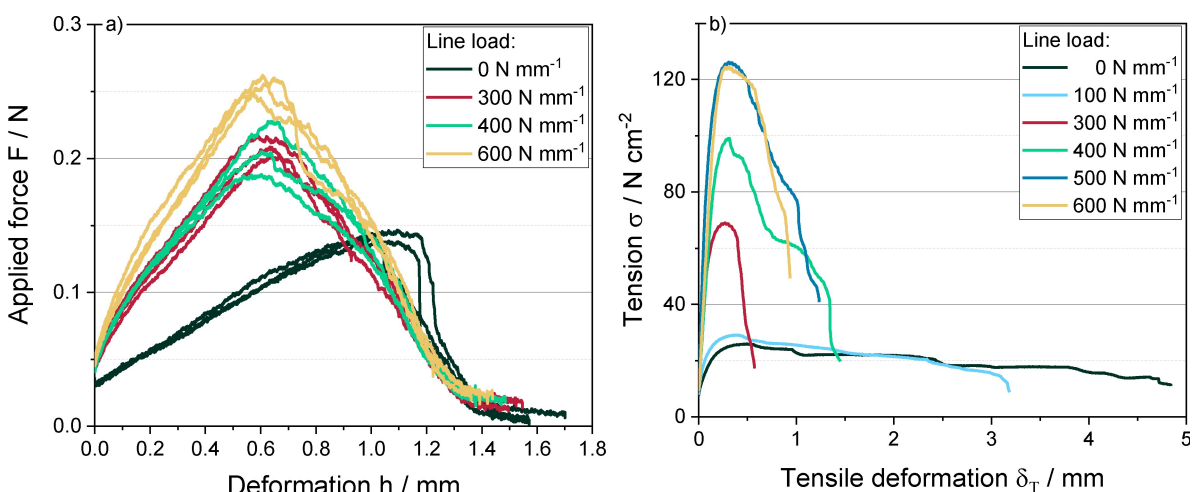


Figure 7. a) Nail penetration test for non-calendered and calendered separators. Roller circumferential speed was kept to 1.0 m min^{-1} and roll temperature to 40°C . Three samples were measured for each line load. b) Tensile measurement for non-calendered and calendered separators. Roller circumferential speed was kept to 1.0 m min^{-1} and roll temperature to 40°C . One sample was measured for each line load.

such as described for polyolefin-based separators for good process handling.^[52,53]

In the next step, different roller circumferential speeds and roll temperatures were investigated in terms of nail penetration tests and tensile strength, and the results are presented in Figure 8a) and b), respectively. The line load was kept constant at 300 N mm^{-1} . For the nail penetration tests, the absorbed force for samples calendered at 60°C (with 60°C and 1.0 m min^{-1} as an exception) or 80°C was increased compared to 40°C . However, no significant differences were observed in the results obtained for 60°C and 80°C at different roller circumferential speeds. In terms of tensile strength, an increase in the roll temperature results in an enlargement of possible stretching of the material. By that, also the absorbed stress is increased. According to this analysis, calendering at elevated temperatures would be desirable. Furthermore, only slight

differences for the different roller circumferential speeds on stretching or stress were observed.

Scanning electron microscopy analysis

As examples, SEM images of the separator surfaces for non-calendered state and calendered states for 300 N mm^{-1} and 600 N mm^{-1} are shown in Figure 9. Surface roughness and open pores within the electrolyte layer have a significant impact on the contact between the separator and electrodes.^[19] SEM images confirm an increase in coating density and a decrease in surface roughness by increased line load. Moreover, scrapes caused by the calender rolls can be seen on the calendered layers additionally modulating the surface.

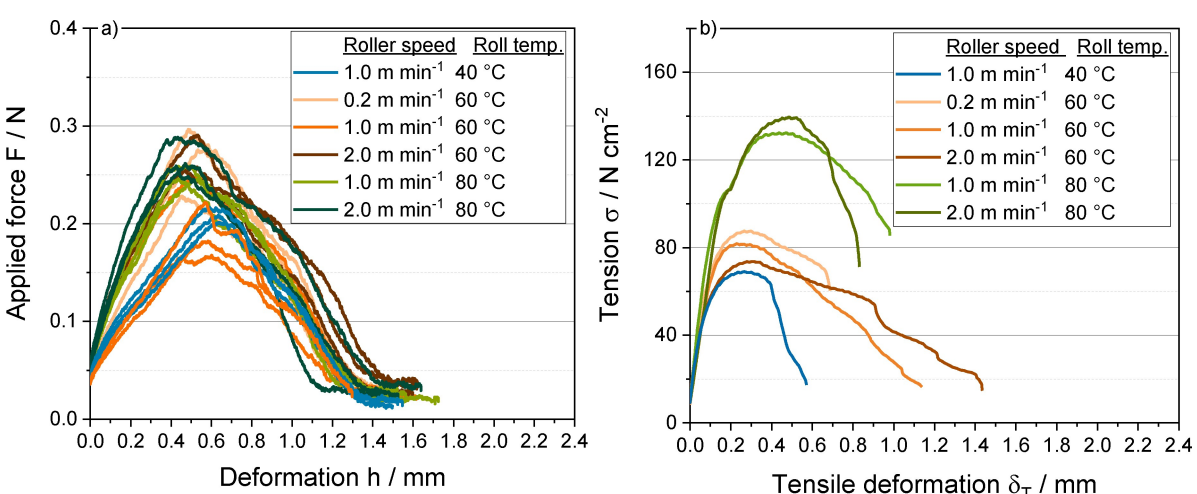


Figure 8. a) Results of nail penetration test for different roll temperatures and roller circumferential speeds. Line load was kept to 300 N mm^{-1} . Three samples were measured for each parameter variation. b) Tensile measurement for calendered separators at different roll temperatures and roller speeds. Line load was kept to 300 N mm^{-1} . One sample was measured for each parameter variation.

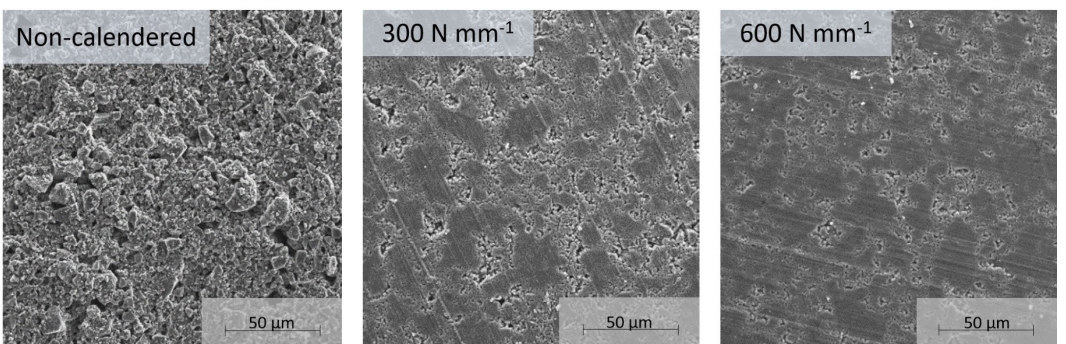


Figure 9. SEM images of the surface of LPSCI separators calendered at different line loads, a roll temperature of 40 °C and a roller circumferential speed of 1.0 m min⁻¹.

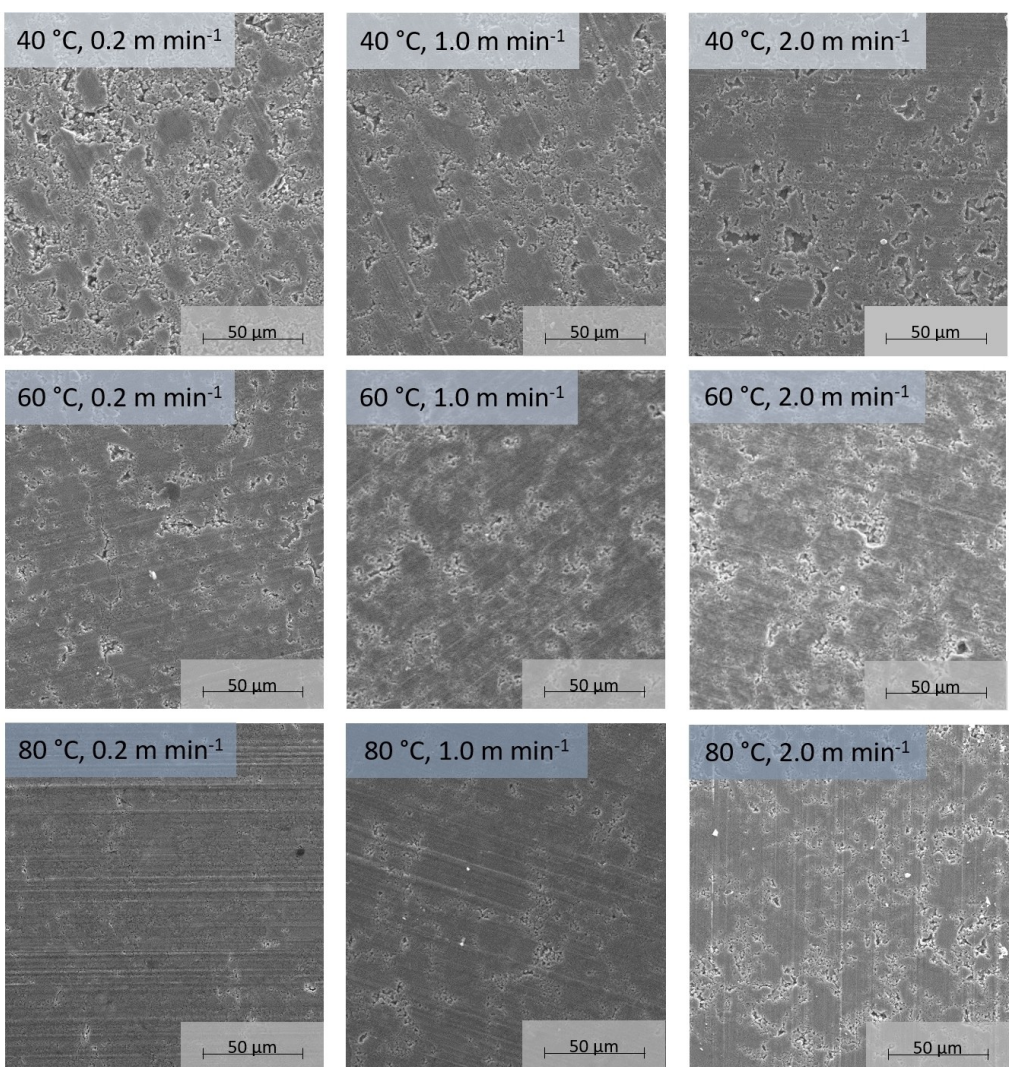


Figure 10. SEM images of LPSCI separator surface for different roll temperatures and roller circumferential speeds. Calendering was performed at a line load of 300 N mm⁻¹.

In Figure 10 SEM images of LPSCI separator calendered at 300 N mm⁻¹ for different roll temperatures (40 °C, 60 °C, 80 °C) in combination with different roller circumferential speeds (0.2 m min⁻¹, 1.0 m min⁻¹, 2.0 m min⁻¹) are presented.

As the measurement of the coating density indicates, a decrease of the roller circumferential speed does have the strongest impact on the resulting layer surface structure for 80 °C in the observed temperature range, while no significant difference in the separator structure can be seen for 40 °C and

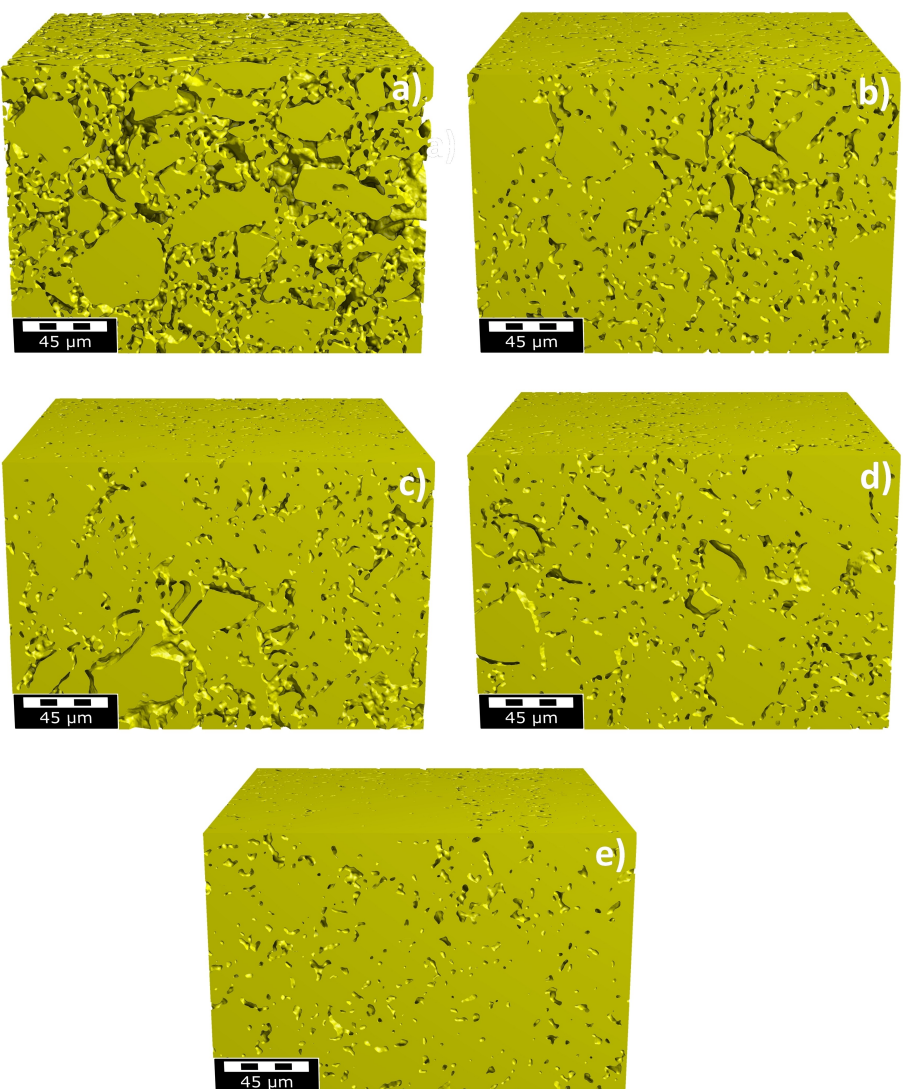


Figure 11. 3D images of the separator structures revealed by synchrotron tomography. Binarization was calibrated according to the geometrically determined porosity. a) Non-calendered sample and samples calendered b) at $300 \text{ N mm}^{-1}/40^\circ\text{C}$, c) $600 \text{ N mm}^{-1}/40^\circ\text{C}$, d) $300 \text{ N mm}^{-1}/60^\circ\text{C}$, as well as e) $300 \text{ N mm}^{-1}/80^\circ\text{C}$ with a roller circumferential speed of 1.0 m min^{-1} .

60°C . Scratches caused by the calender rolls occur more strongly with increased roll temperature.

Structural analysis

Figure 11 illustrates the 3D images of the separator structures in both non-calendered state and calendered states at $300 \text{ N mm}^{-1}/40^\circ\text{C}$, at $600 \text{ N mm}^{-1}/40^\circ\text{C}$, at $300 \text{ N mm}^{-1}/60^\circ\text{C}$ and $300 \text{ N mm}^{-1}/80^\circ\text{C}$. The separators were calendered at a roller circumferential speed of 1.0 m min^{-1} .

The specific surface area estimated for the samples shown in Figure 11 is demonstrated in Table 4.^[54] The specific surface area of the sample calendered at 300 N mm^{-1} is reduced by 38% and for 600 N mm^{-1} by 41% compared to non-calendered state. The specific surface area of the layer calendered at 80°C is reduced by 40%.

Table 4. Estimated surface area. Separators were calendered with a roller circumferential speed of 1.0 m min^{-1} .

| Line load/ N mm^{-1} | Roll temperature/ $^\circ\text{C}$ | Spec. surface area/ $\text{m}^2 \text{ m}^{-3}$ |
|-------------------------------|------------------------------------|---|
| Non-calendered | Non-calendered | 331 436 |
| 300 | 40 | 206 874 |
| 600 | 40 | 197 051 |
| 300 | 60 | 224 501 |
| 300 | 80 | 199 379 |

Segmented images are shown in Figure 12 for non-calendered state and for 300 N mm^{-1} at 40°C , 60°C and 80°C , as well as for 600 N mm^{-1} at 40°C . The unedited images are shown in the Supporting Information in Figure S.4. Particle breakage is observed for all calendered samples. In literature, particle breakage due to calendering is already described for other materials such as secondary cathode active material

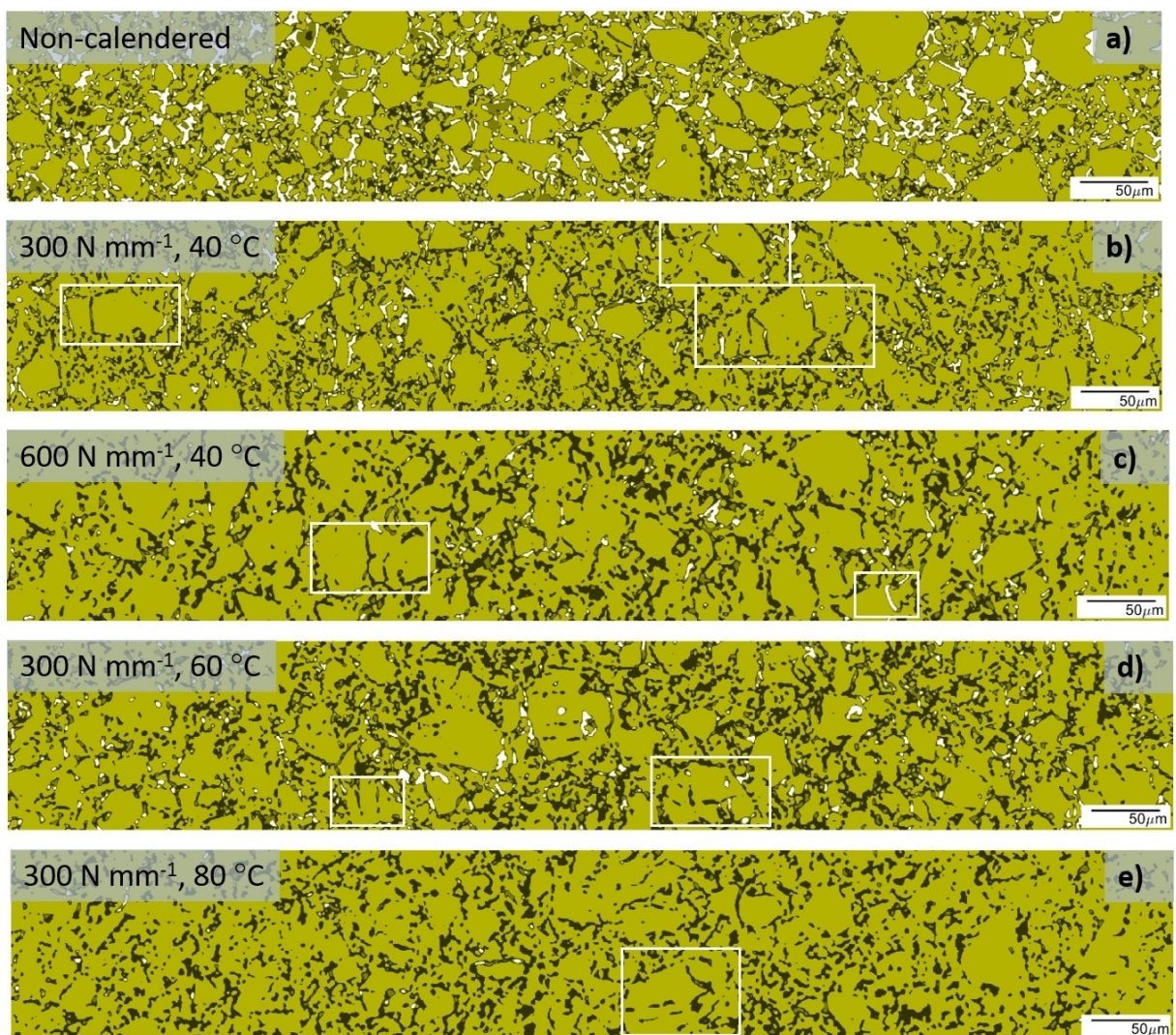


Figure 12. Segmented images of samples a) in non-calendered state, b) calendered at $300 \text{ N mm}^{-1}/40^\circ\text{C}$, c) $600 \text{ N mm}^{-1}/40^\circ\text{C}$, d) $300 \text{ N mm}^{-1}/60^\circ\text{C}$, as well as e) $300 \text{ N mm}^{-1}/80^\circ\text{C}$. Examples of particle breakage are outlined by white rectangles.

particles.^[55,56] Because high-stress load concentrates on coarser particles within the layer and small particles are more likely to escape into voids, coarser particles are more prone to cracking. Moreover, decreasing the particle size usually increases particle strength.^[57–59] This particle breakage probably results in additional interfaces and thus, a slight increase in the internal resistance within the separator. Possible solutions to minimize particle breakage might be the usage of a sulfide material with a more homogeneous particle size distribution and a smaller particle size. For example, by *in situ* imaging lithiation-induced failure for $\text{Li}_{10}\text{GeP}_2\text{S}_{12}$ particles greater than 3 μm fracturing was always observed, between 1 μm and 3 μm microcracks occasionally occurred and for <1 μm no chemo-mechanical failure was observed.^[60] However, small particle size also results in a high surface area and therefore, probably in high ionic interfacial resistance but is also associated with low surface roughness.^[19] Particle size could be reduced by ball-milling, for instance.^[27] Here, particles are fragmented before the microstructure is formed after solvent evaporation in contrast to

particles that break during calendering. In future studies, particle breakage should be quantified for different line loads and roll temperatures.

Specific ionic conductivity

Figure 13 a) presents the specific ionic conductivity measured at 25 °C and 25 MPa for different line loads applied to the separators. Ionic resistance (absolute value) is shown in Figure S.5 in the Supporting Information. Unexpectedly, no increase in the specific ionic conductivity but a slight decrease leading to an almost constant level was obtained. Accordingly, the absolute ionic resistance increases at first and then approaches a constant level. These results contrast the confirmation of a defined densification of the layers by measurements of density, tensile strength, nail penetration, as well as SEM analysis. Moreover, these findings differ from those

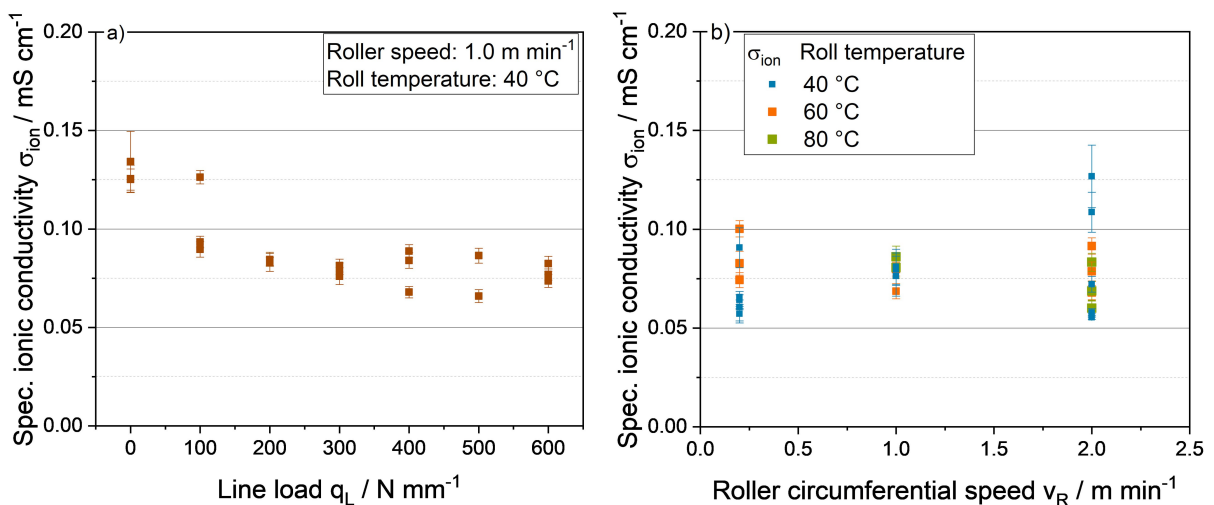


Figure 13. Specific ionic conductivity a) as a function of the line load, b) as a function of the roller circumferential speed for different roll temperatures. Individual measurement data points are shown. Standard deviation is based on the variation of the layer thickness for the measured sample, as well as on the fit error for the applied model given by RelaxIS.

obtained for an increase in fabrication pressures applied to sulfide electrolyte powder.^[16]

Furthermore, the specific ionic conductivity was measured for different roll temperatures and roller circumferential speeds and a line load of 300 N mm^{-1} (Figure 13b)). Here, no significant impact was obtained despite the achievement of a slightly higher density for a roll temperature of 80°C .

To clarify whether this trend in ionic conductivity is due to calendering itself, experiments with a uniaxial press were conducted. Here, different approaches were investigated as listed in Table 5. For Series 1 and 2, the separators were compacted by uniaxial pressing at different fabrication pressures at 40°C and 100°C , respectively. Afterwards, the impedance was measured at a stack pressure of 25 MPa . The according specific ionic conductivity is shown in Figure 14a) as

a function of the fabrication pressure also including the specific ionic conductivity obtained for calendering as a function of the line load (Series 5). Moreover, different constant stack pressures were applied to non-compacted separators during impedance spectroscopy measurement (Series 3). For Series 4, separators were compacted at different fabrication pressures. The stack pressure during the measurement of impedance spectroscopy equaled the fabrication pressure. For example, impedance spectroscopy for separators pre-compacted at 100 MPa was also measured at 100 MPa . For Series 6, a separator was calendered at 300 N mm^{-1} , 40°C and 1.0 m min^{-1} and impedance spectroscopy was performed for different stack pressures. The results in terms of the specific ionic conductivity as a function of the stack pressure are shown in Figure 14b).

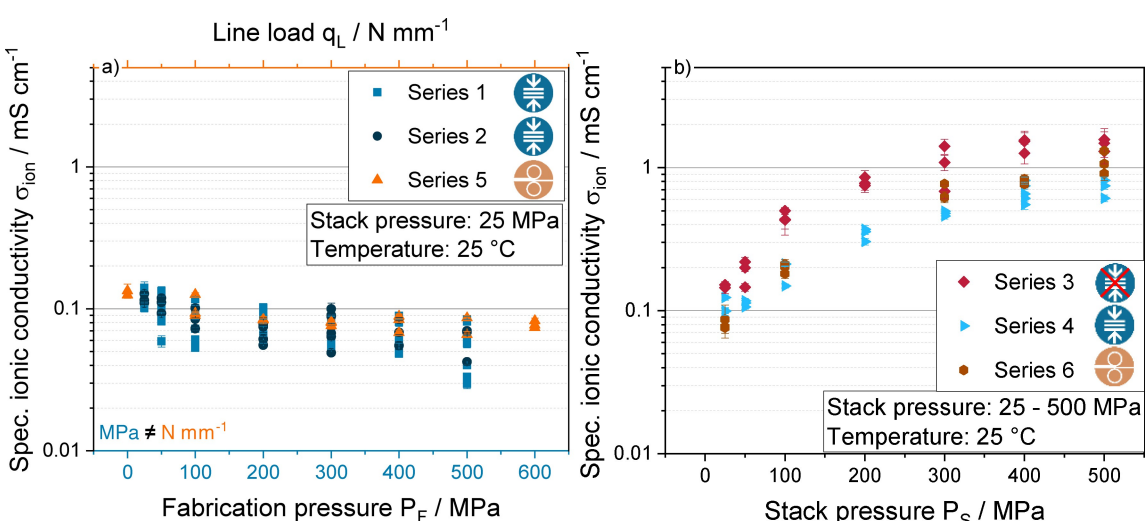


Figure 14. Specific ionic conductivities of LPSCI separators for a) different fabrication pressures or line loads measured at a stack pressure of 25 MPa , b) different stack pressures applied to non-compacted, compacted or calendered separators (see Table 5). Individual measurement data points are shown. Standard deviation is based on the variation of the layer thickness for the measured sample, as well as on the fit error for the applied model given by RelaxIS.

Table 5. Measurement series that were analyzed by electrochemical impedance spectroscopy.

| Series | Fabrication pressure/MPa | Fabrication temp./°C | Stack pressure/MPa | Measurement temp./°C |
|--------|----------------------------------|----------------------|------------------------|-------------------------|
| 1 | 25 | 40 | 25 | 25 |
| | 50 | 40 | 25 | |
| | 100 | 40 | 25 | |
| | 200 | 40 | 25 | |
| | 300 | 40 | 25 | |
| | 400 | 40 | 25 | |
| | 500 | 40 | 25 | |
| | 25 | 100 | 25 | |
| 2 | 50 | 100 | 25 | 25 |
| | 100 | 100 | 25 | |
| | 200 | 100 | 25 | |
| | 300 | 100 | 25 | |
| | 400 | 100 | 25 | |
| 3 | 500 | 100 | 25 | 25 |
| | Non-compacted | — | 25 | |
| | Non-compacted | — | 50 | |
| | Non-compacted | — | 100 | |
| | Non-compacted | — | 200 | |
| | Non-compacted | — | 300 | |
| | Non-compacted | — | 400 | |
| | Non-compacted | — | 500 | |
| | 25 | 40 | 25 | |
| | 50 | 40 | 50 | |
| 4 | 100 | 40 | 100 | 25 |
| | 200 | 40 | 200 | |
| | 300 | 40 | 300 | |
| | 400 | 40 | 400 | |
| | 500 | 40 | 500 | |
| | | | | |
| Series | Line load/ N mm ⁻¹ | Roll temp./ °C | Stack pressure/ MPa | Measurement temp./°C |
| 5 | 100 | 40 | 25 | 25 |
| | 200 | 40 | 25 | |
| | 300 | 40 | 25 | |
| | 400 | 40 | 25 | |
| | 500 | 40 | 25 | |
| | 600 | 40 | 25 | |
| 6 | 300 | 40 | 25 | 25 |
| | 300 | 40 | 100 | |
| | 300 | 40 | 300 | |
| | 300 | 40 | 400 | |
| | 300 | 40 | 500 | |

A slight decrease in the specific ionic conductivity is also obtained for an increase in the uniaxial fabrication pressure (Series 1 and 2). However, the results obtained for uniaxial pressing cannot be directly compared to the results for

calendering because an estimation of the resulting pressure onto the separator within the calender gap is complex. An increase in stack pressure for non-compacted separators results in the expected increase of specific ionic conductivity (Series 3)

due to improved particle contact,^[61,62] as well as due to improved contact with the metal plungers.^[16]

This is also true for the combination of fabrication pressure and the same stack pressure during the impedance measurement (Series 4) but lower compared to results from Series 3. This also applies to the calendered samples (Series 6) indicating that a pre-densification somehow negatively affects the microstructure of the separator that cannot be fully compensated by the application of a high stack pressure within the observed pressure range.

In conclusion, the slight decrease of specific ionic conductivity with increasing densification degree is not due to calendering itself but probably due to the general effects of pre-densification on the tested separators. In contrast to the results found in this study, Doux et al.^[16] tested different fabrication pressures for LPSCI powder (same supplier) obtaining an increase in the specific ionic conductivity with an increase in the fabrication pressure. Impedance was also measured at 25 MPa. However, they used carbon powder as current collector for impedance measurement achieving a better contact interface compared to metal plungers used in this study (see discussion below).^[16] Also, they compacted pure LPSCI powder. In the present study, slurry-based separators were produced based on an HNBR binder. Consequently, it is assumed that a spring back effect by fast elastic recovery probably mainly caused by the binder after tension release could have a negative impact on the microstructure of the separator in terms of lithium-ion transportation. The spring back effect after calendering has already been discussed for conventional electrodes.^[24,63–65]

Sedlmeier et al.^[29] also compacted LPSCI (different supplier) separator sheets based on an HNBR binder different from the one used in this study with a content of 5 wt% in the separator layer. They described a 2-fold higher ionic conductivity for a separator non-compacted measured at a stack pressure of 590 MPa compared to a sample compacted at 590 MPa and measured at a stack pressure of 70 MPa despite having the same porosity of ≈3%. They also assume a spring back resulting in a microscopic contact loss of the sulfidic particles or higher contact resistance at low stack pressure. Moreover, they only found a significant increase in the ionic conductivity for porosities lower than 10% measured at a stack pressure of 70 MPa. In contrast to this study, all pre-compacted separators showed slightly higher ionic conductivity compared to non-pre-compacted separators measured at the same stack pressure. Reasons amongst others might be the usage of another HNBR binder type and/or an LPSCI material with probably a different particle size distribution. Moreover, the ionic conductivity was measured in the same cell body that was used for the densification. Thus, better contact with the metal plungers can be expected.

In addition, an increase in the ionic conductivity was also found by Doux et al. for LPSCI pellets compacted at 370 MPa with an increase of the stack pressure attributed to improved contacting between the pellet and metal current collectors based on titanium and minimized contact impedance.^[16,29] Thus, the contact interface between LPSCI and the plunger also

significantly depends on the stack pressure.^[16] Consequently, an increase in the stack pressure results in improved contacting additionally improving the measured ionic conductivity. They recommend carbon powder as current collector for EIS measurement.^[16] In customer applications usually only low stack pressures can be realized.

Based on the results found by Sedlmeier et al.^[29] and Doux et al.^[16] the specific ionic conductivity was also measured for LPSCI separators at a stack pressure of 70 MPa compared to 25 MPa (see Figure 15). For a stack pressure of 70 MPa the specific ionic conductivity is decreased from non-compacted separators to separators compacted at 100 MPa followed by a slight increase for a fabrication pressure of 300 MPa and 500 MPa. The non-compacted samples still have a higher ionic conductivity compared to separators in compacted state despite higher stack pressure. Moreover, the ionic conductivity for a stack pressure of 70 MPa and uniaxial densification of 500 MPa (0.19 mS cm^{-1} , second-best value out of three) still is approximately 8 times smaller compared to a separator in non-compacted state and a stack pressure of 500 MPa (1.48 mS cm^{-1} , second-best value out of three) that eventually cannot be explained only by better contacting to the plungers.

The hypothesis of a negative effect on the separator microstructure by elastic deformation after densification has to be confirmed by further studies to reveal the complex correlations between uniaxial pressing or calendering and the application of stack pressure. For example, by varying the binder content or testing alternative binders because different deformation behavior can be expected.^[66] In this context, also the impact of particle breakage caused by densification on the separator performance has to be investigated in more detail, as well as the impact of particle size of the electrolyte material and the deformation behavior of the particles themselves. Another approach could be an investigation of the chemical interactions between the electrolyte material and binder.^[67] For the separators produced in this study in terms of ionic performance

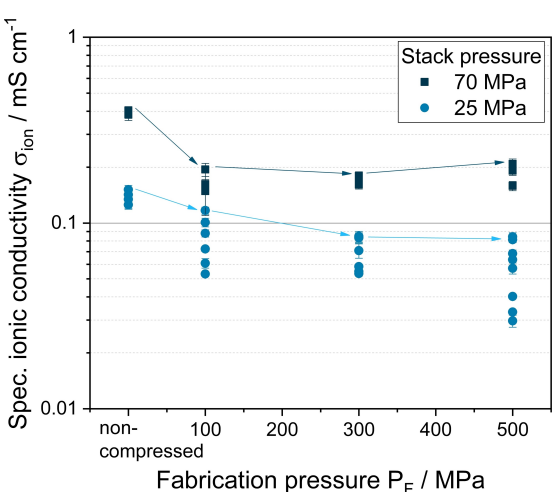


Figure 15. Specific ionic conductivity as a function of the fabrication pressure measured at a stack pressure of 25 MPa compared to 70 MPa. Individual measurement data points are shown. Standard deviation is based on the variation of the layer thickness for the measured sample, as well as on the fit error for the applied model given by RelaxIS.

a pre-densification by pressing or calendering seems rather unfavorable.

Conclusion

In this study, the effects of calendering on slurry-based LPS and LPSCI layers were investigated systematically in terms of line load, roll temperature and roller speed. The following main findings were identified for the electrolyte materials tested in this study:

- Separators based on LPS showed high brittleness in calendered state. In contrast, for LPSCI free-standing separators could be obtained for further analysis and processing.
- Higher initial layer thicknesses result in the achievement of a slightly higher coating density, but also in higher compaction resistance. Moreover, thinner separators were more fragile complicating processing.
- Increased roll temperature in combination with decreased roller circumferential speed increased length expansion, as well as layer fragmentation.
- Particle breakage was observed for all calendered separators revealed by synchrotron tomography.
- An increase in applied line load leads to a denser structure but a slight decrease in the specific ionic conductivity for a stack pressure of 25 MPa. This was also found for separators compacted by a uniaxial press. A possible reason might be an elastic deformation of the binder-based separators after tension release negatively affecting the microstructure of the separator. Maybe the deformation behavior of the tested HNBR binder is not compatible with the deformation behavior of the LPSCI. An increase of stack pressure applied at impedance spectroscopy itself increased the specific ionic conductivity.
- If confirmed in further studies, the elastic deformation of the individual components after densification is a highly relevant material characteristic for SSBs due to the high importance of good interface contact. The effect of spring back, as well as the impact of particle breakage, has to be investigated in more detail. An impact on the performance due to this phenomenon probably can also be expected for composite anodes or cathodes and has to be evaluated in future studies.

This study provides first important insights into the calendering of sulfide-based separators for an application in SSBs but also raises numerous hypotheses that have to be addressed in future research such as the deformation behavior of separators after densification.

Acknowledgements

We thank the German Federal Ministry of Research and Education for the financial support (BiSSFest – 03XP0412A). We also thank Anne-Katrin Landa, Ran Duan and Zhaoxian Ye for experimental support, as well as Rose Karimi, Lennart Blume,

Kevin Voges and Mattis Batzer for helpful discussions. Thank you to Dominik Steckermeier for providing the separator formulation. Open Access funding enabled and organized by Projekt DEAL.

Conflict of Interests

The authors declare no conflict of interest.

Data Availability Statement

The data that support the findings of this study are available from the corresponding author upon reasonable request.

Keywords: All-solid-state batteries · calendering · electrolyte material · sulfides

- [1] A. Kwade, W. Haselrieder, R. Leithoff, A. Modlinger, F. Dietrich, K. Droeder, *Nat. Energy* **2018**, *3*, 290.
- [2] J. Janek, W. G. Zeier, *Nat. Energy* **2023**, *8*, 230.
- [3] J. Janek, W. G. Zeier, *Nat. Energy* **2016**, *1*, 16141.
- [4] F. Duffner, N. Kronemeyer, J. Tübke, J. Leker, M. Winter, R. Schmuck, *Nat. Energy* **2021**, *6*, 123.
- [5] A. Manthiram, X. Yu, S. Wang, *Nat. Rev. Mater.* **2017**, *2*, 16103.
- [6] M. Batzer, C. Heck, P. Michalowski, A. Kwade, *Batteries & Supercaps* **2022**, *5*, e202200328.
- [7] C. Singer, H.-C. Töpper, T. Kutsch, R. Schuster, R. Koerver, R. Daub, *ACS Appl. Mater. Interfaces* **2022**, *14*, 24245.
- [8] M. Batzer, K. Voges, W. Wang, P. Michalowski, A. Kwade, *Mater. Today Commun.* **2022**, *30*, 103189.
- [9] Y.-G. Lee, S. Fujiki, C. Jung, N. Suzuki, N. Yashiro, R. Omoda, D.-S. Ko, T. Shiratsuchi, T. Sugimoto, S. Ryu, J. H. Ku, T. Watanabe, Y. Park, Y. Aihara, D. Im, I. T. Han, *Nat. Energy* **2020**, *5*, 299.
- [10] S. Ito, S. Fujiki, T. Yamada, Y. Aihara, Y. Park, T. Y. Kim, S.-W. Baek, J.-M. Lee, S. Doo, N. Machida, *J. Power Sources* **2014**, *248*, 943.
- [11] J. Schnell, T. Günther, T. Knoche, C. Vieider, L. Köhler, A. Just, M. Keller, S. Passerini, G. Reinhart, *J. Power Sources* **2018**, *382*, 160.
- [12] J. Lee, T. Lee, K. Char, K. J. Kim, J. W. Choi, *Acc. Chem. Res.* **2021**, *54*, 3390.
- [13] M. Batzer, D. Gundlach, P. Michalowski, A. Kwade, *ChemElectroChem* **2023**, *10*, e202300452.
- [14] R. Koerver, I. Aygün, T. Leichtweiß, C. Dietrich, W. Zhang, J. O. Binder, P. Hartmann, W. G. Zeier, J. Janek, *Chem. Mater.* **2017**, *29*, 5574.
- [15] T. Ates, M. Keller, J. Kulisch, T. Adermann, S. Passerini, *Energy Storage Mater.* **2019**, *17*, 204.
- [16] J.-M. Doux, Y. Yang, D. H. S. Tan, H. Nguyen, E. A. Wu, X. Wang, A. Banerjee, Y. S. Meng, *J. Mater. Chem. A* **2020**, *8*, 5049.
- [17] R. Garcia-Mendez, J. G. Smith, J. C. Neufeld, D. J. Siegel, J. Sakamoto, *Adv. Energy Mater.* **2020**, *10*, 2000335.
- [18] S. Randau, D. A. Weber, O. Kötz, R. Koerver, P. Braun, A. Weber, E. Ivers-Tiffée, T. Adermann, J. Kulisch, W. G. Zeier, F. H. Richter, J. Janek, *Nat. Energy* **2020**, *5*, 259.
- [19] D. K. Singh, A. Henss, B. Mogwitz, A. Gautam, J. Horn, T. Krauskopf, S. Burkhardt, J. Sann, F. H. Richter, J. Janek, *Cell Rep. Phys. Sci.* **2022**, *3*, 101043.
- [20] C. Meyer, M. Weyhe, W. Haselrieder, A. Kwade, *Energy Technol.* **2020**, *8*, 1900175.
- [21] C. Meyer, H. Bockholt, W. Haselrieder, A. Kwade, *J. Mater. Process. Technol.* **2017**, *249*, 172.
- [22] Y. Sheng, C. R. Fell, Y. K. Son, B. M. Metz, J. Jiang, B. C. Church, *Front. Energy Res.* **2014**, *2*, 56.
- [23] W. Haselrieder, S. Ivanov, D. K. Christen, H. Bockholt, A. Kwade, *ECS Trans.* **2013**, *50*, 59.
- [24] A. Diener, S. Ivanov, W. Haselrieder, A. Kwade, *Energy Technol.* **2022**, *10*, 2101033.

- [25] N. Riphaus, P. Strobl, B. Stiaszny, T. Zinkevich, M. Yavuz, J. Schnell, S. Indris, H. A. Gasteiger, S. J. Sedlmaier, *J. Electrochem. Soc.* **2018**, *165*, A3993.
- [26] S. Kim, Y. A. Chart, S. Narayanan, M. Pasta, *Nano Lett.* **2022**, *22*, 10176.
- [27] D. J. Lee, J. Jang, J.-P. Lee, J. Wu, Y.-T. Chen, J. Holoubek, K. Yu, S.-Y. Ham, Y. Jeon, T.-H. Kim, J. B. Lee, M.-S. Song, Y. S. Meng, Z. Chen, *Adv. Funct. Mater.* **2023**, *33*, 2301341.
- [28] Z. Zhang, L. Wu, D. Zhou, W. Weng, X. Yao, *Nano Lett.* **2021**, *21*, 5233.
- [29] C. Sedlmeier, T. Kutsch, R. Schuster, L. Hartmann, R. Bublitz, M. Tominac, M. Bohn, H. A. Gasteiger, *J. Electrochem. Soc.* **2022**, *169*, 070508.
- [30] A. Tron, R. Hamid, N. Zhang, A. Paolella, P. Wulfert-Holzmann, V. Kolotygin, P. López-Aranguren, A. Beutl, *J. Energy Storage* **2023**, *66*, 107480.
- [31] C. Meyer, M. Kosfeld, W. Haselrieder, A. Kwade, *J. Energy Storage* **2018**, *18*, 371.
- [32] R. W. Heckel, *Trans. Metall. Soc. AIME* **1961**, *221*, 671.
- [33] J. Auvergniot, A. Cassel, J.-B. Ledueil, V. Viallet, V. Seznec, R. Dedryvère, *Chem. Mater.* **2017**, *29*, 3883.
- [34] N. Kamaya, K. Homma, Y. Yamakawa, M. Hirayama, R. Kanno, M. Yonemura, T. Kamiyama, Y. Kato, S. Hama, K. Kawamoto, A. Mitsui, *Nat. Mater.* **2011**, *10*, 682.
- [35] Z. Liu, W. Fu, E. A. Payzant, X. Yu, Z. Wu, N. J. Dudney, J. Kiggans, K. Hong, A. J. Rondinone, C. Liang, *J. Am. Chem. Soc.* **2013**, *135*, 975.
- [36] F. Marchini, B. Porcheron, G. Rousse, L. Albero Blanquer, L. Droguet, D. Foix, T. Koç, M. Deschamps, J. M. Tarascon, *Adv. Energy Mater.* **2021**, *11*, 2101111.
- [37] M. Dixit, N. Muralidharan, A. Parejiya, C. Jafta, Z. Du, S. M. Neumayer, R. Essehli, R. Amin, M. Balasubramanian, I. Belharouak, *ACS Appl. Mater. Interfaces* **2022**, *14*, 44292.
- [38] M. Ghidiu, J. Ruhl, S. P. Culver, W. G. Zeier, *J. Mater. Chem. A* **2019**, *7*, 17735.
- [39] P. Minnmann, L. Quillman, S. Burkhardt, F. H. Richter, J. Janek, *J. Electrochem. Soc.* **2021**, *168*, 040537.
- [40] S. Yanev, H. Auer, C. Heubner, S. Höhn, K. Nikolowski, M. Partsch, A. Michaelis, *J. Electrochem. Soc.* **2022**, *169*, 090519.
- [41] L. Froboese, P. Titscher, B. Westphal, W. Haselrieder, A. Kwade, *Mater. Charact.* **2017**, *133*, 102.
- [42] H. Markötter, M. Sintschuk, R. Britzke, S. Dayani, G. Bruno, *J. Synchrotron Radiat.* **2022**, *29*, 1292.
- [43] C. A. Schneider, W. S. Rasband, K. W. Eliceiri, *Nat. Methods* **2012**, *9*, 671.
- [44] J. Schindelin, I. Arganda-Carreras, E. Frise, V. Kaynig, M. Longair, T. Pietzsch, S. Preibisch, C. Rueden, S. Saalfeld, B. Schmid, J.-Y. Tinevez, D. J. White, V. Hartenstein, K. Eliceiri, P. Tomancak, A. Cardona, *Nat. Methods* **2012**, *9*, 676.
- [45] W. van Aarle, W. J. Palenstijn, J. Cant, E. Janssens, F. Bleichrodt, A. Dabrowski, J. de Beenhouwer, K. Joost Batenburg, J. Sijbers, *Opt. Express* **2016**, *24*, 25129.
- [46] W. J. Palenstijn, K. J. Batenburg, J. Sijbers, *J. Struct. Biol.* **2011**, *176*, 250.
- [47] F. P. McGrogan, T. Swamy, S. R. Bishop, E. Eggleton, L. Porz, X. Chen, Y.-M. Chiang, K. J. van Vliet, *Adv. Energy Mater.* **2017**, *7*, 1602011.
- [48] Z. Miao, T. E. Grift, K. C. Ting, *Encycl. Agric. Food Biol. Eng* **2014**.
- [49] J. Wu, S. Liu, F. Han, X. Yao, C. Wang, *Adv. Mat.* **2021**, *33*, 2000751.
- [50] G. Liu, J. Shi, M. Zhu, W. Weng, L. Shen, J. Yang, X. Yao, *Energy Storage Mater.* **2021**, *38*, 249.
- [51] J. Malac, *TOMACROJ* **2009**, *3*, 41.
- [52] Q. Wang, *Electrochim. Acta* **2015**, *182*, 334.
- [53] W. Zhao, Z. Guo, Z. Ma, S. Wang, S. Yang, J. Liu, H. Zhao, L. Ren, *ACS Appl. Mater. Interfaces* **2023**, *15*, 41783.
- [54] J. Ohser, F. Mücklich, *Statistical analysis of microstructures in materials science*, Wiley and Sons **2000**, p. 115.
- [55] C. A. Heck, F. Huttner, J. K. Mayer, O. Fromm, M. Börner, T. Heckmann, P. Scharfer, W. Schabel, M. Winter, A. Kwade, *Energy Technol.* **2023**, *11*, 2200945.
- [56] F. Huttner, A. Diener, T. Heckmann, J. C. Eser, T. Abali, J. K. Mayer, P. Scharfer, W. Schabel, A. Kwade, *J. Electrochem. Soc.* **2021**, *168*, 090539.
- [57] K. Schönert, *Aufbereitungs-Technik* **1991**, *32*, 487.
- [58] S. Breitung-Faes, A. Kwade, *Miner. Eng.* **2013**, *43–44*, 36.
- [59] H. Rumpf, *Chem. Ing. Tech.* **1965**, *37*, 187.
- [60] J. Zhao, C. Zhao, J. Zhu, X. Liu, J. Yao, B. Wang, Q. Dai, Z. Wang, J. Chen, P. Jia, Y. Li, S. J. Harris, Y. Yang, Y. Tang, L. Zhang, F. Ding, J. Huang, *Nano Lett.* **2022**, *22*, 411.
- [61] A. Sakuda, A. Hayashi, M. Tatsumisago, *Sci. Rep.* **2013**, *3*, 2261.
- [62] M. Nose, A. Kato, A. Sakuda, A. Hayashi, M. Tatsumisago, *J. Mater. Chem. A* **2015**, *3*, 22061.
- [63] M. Abdollahifar, H. Cavers, S. Scheffler, A. Diener, M. Lippke, A. Kwade, *Adv. Energy Mater.* **2023**, *13*, 2300973.
- [64] D. Schreiner, A. Klinger, G. Reinhart, *Procedia CIRP* **2020**, *93*, 149.
- [65] J. Xu, B. Paredes-Goyes, Z. Su, M. Scheel, T. Weitkamp, A. Demortière, A. A. Franco, *Batteries & Supercaps* **2023**, *6*, e202300371.
- [66] Y.-S. Park, E.-S. Oh, S.-M. Lee, *J. Power Sources* **2014**, *248*, 1191.
- [67] J. Choi, J. Y. Kim, S. H. Kang, D. O. Shin, M. J. Lee, Y.-G. Lee, *J. Mater. Chem. A* **2024**, advance article.

Manuscript received: October 19, 2023

Revised manuscript received: January 2, 2024

Accepted manuscript online: January 8, 2024

Version of record online: February 19, 2024